Quantitative assessment of network depolymerization in archetypal superionic glasses and its relationship with ion conduction: A case study on Na_2S-GeS_2

M. Micoulaut,[1] A. Piarristeguy,[2] O. Masson,[3] L.-M. Poitras,[1] R. Escalier,[2] A. Kachmar,[4,5] and A. Pradel[2]
[1]Sorbonne Université, Laboratoire de Physique Théorique de la Matière Condensée, CNRS UMR 7600,
4 Place Jussieu, 75252 Paris Cedex 05, France
[2]ICGM, Université de Montpellier, CNRS, ENSCM, 34293 Montpellier, France
[3]Institut de Recherche sur les Céramiques, UMR 7315 CNRS-Université de Limoges, Centre Européen de la Céramique,
12 rue Atlantis 87068 Limoges Cedex, France
[4]Department of Physics, College of Science, Sultan Qaboos University, P.O. Box 36, P.C. 123, Muscat, Oman
[5]Computational Laboratory for Hybrid/Organic Photovoltaics (CLHYO), Istituto CNR di Scienze e Tecnologie Chimiche "Giulio Natta"
(CNR-SCITEC), Via Elce di Sotto 8, 06123 Perugia, Italy

(Received 4 July 2023; revised 2 October 2023; accepted 5 October 2023; published 24 October 2023)

The properties of xNa$_2$S-(100-x)GeS$_2$ glasses, which represent promising systems for all-solid-state batteries, are thoroughly investigated from a variety of experimental and theoretical techniques. The ionic conduction is measured as a function of composition. It reveals a powerlike behavior with a threshold composition found at low Na content. In contrast, temperature evolution suggests a typical Arrhenius behavior indicative of Na motions achieved by jumps between neighboring sites. Three particular compositions (0%, 33%, and 66% Na$_2$S) are characterized by a combination of x-ray diffraction and density functional based molecular dynamics. Different structural properties are measured and calculated, such as structure factors, pair distribution functions, angular distributions, coordination numbers, and neighbor distributions. The comparison with experiments reveals a rather good agreement in real and reciprocal space. The short-range order is found to consist of a base network made of GeS$_{4/2}$ tetrahedra (with Ge and S coordination numbers being of about 4 and 2) that are progressively depolymerized upon Na addition that also leads to a breakdown of the ring structure. Na coordination numbers are loosely defined, especially at high Na content. Typical features of alkali-modified silicates are also found, such as the presence of channel-like dynamics, a bond-length distribution that is different between Ge and bridging or nonbridging sulfur, a distribution Q^n of Ge tetrahedra having n bonding sulfur, and a decoupling at low temperatures between network species (Ge, S) and Na dynamics. However, unlike such archetypal glasses, sodium thiogermanates contain homopolar Ge-Ge bonds that are specific to Ge chalcogenides and which lead to isolated $(Ge_2S_6)^{6\ominus}$ anions at high Na content.

DOI: 10.1103/PhysRevB.108.144205

I. INTRODUCTION

A carbon-free renewable energy future requires the development of a new generation of electrochemical energy storage systems such as vehicular propulsion, nomad application, and load leveling of temporal renewable energy harvesters such as wind turbines and solar photovoltaic and solar thermal systems [1]. Despite the current success of lithium batteries, their dependence on flammable liquid electrolytes and on a rather expensive element (Li) whose natural abundance is very low requires the development of new battery systems, including batteries using an amorphous electrolyte.

Na-ion all-solid-state batteries are, therefore, a promising alternative to lithium batteries as they would be cheaper and much safer because they would not suffer from leakage, volatilization, or flammability. Sodium has a standard electrode potential comparable to lithium and is among the most abundant elements. However, the development of all-solid-state batteries is challenging. Solid electrode/electrolyte interfaces quickly deteriorate during charge and discharge processes. Another drawback in developing all-solid-state devices is the low conductivity level of solid electrolytes. Among sodium fast-ion conductors, glasses such as Na$_2$S-SiS$_2$ or Na$_2$S-GeS$_2$ appear attractive given the large polarizability of the sulfur atoms and have received some attention, as these materials can accept significant changes in compositions without any vital change in volume.

On the particular Na$_2$S-GeS$_2$ (N-G) system, early experimental studies [2–4] have shown that Na$_2$S can be added to the base glass network former GeS$_2$ from 0% up to 60% by melt-quenching technique, and forms stable glasses with glass transition temperatures between 250 °C–280 °C, and whose tetrahedral character and structure have been characterized by different methods, from spectroscopic [3,5,6] to x-ray and neutron scattering [7,8]. The N-G system whose phase diagram has been characterized [9] seems to display a tendency to phase separation (like in archetypal alkali silicates [10,11]) and devitrification at low modifier content [12] and some elevated annealing temperature (600 °C). As in many other modified oxides or chalcogenides [11,13], elementary building blocks of the glass structure are, indeed, made of so-called Q^n species (i.e., $Na^{(4-n)\oplus}GeS_4^{\ominus}$ tetrahedra) where

$n = 4$ represents the number of bridging sulfur (BS) atoms per Ge tetrahedra in the base glass GeS_2. Upon Na_2S addition, the structure depolymerizes [14], indeed, by creating nonbridging sulfur (NBS) atoms having Na ions in their vicinity. For alkali-rich compositions, this induces structures with more and more Q^1 and isolated Q^0 units (no BS at all), which enhance ionic conduction. The latter property has also been examined at room temperature [4] with composition and an increase in ionic conductivity σ with Na content was acknowledged, as σ increased substantially from 10^{-8} to 10^{-5} $\Omega^{-1}\,cm^{-1}$ between 30% and 60% Na_2S [2]. The evolution with temperature appears to be of Arrhenius type, i.e., $\sigma T \propto \exp[-E_A/KT]$. This result has been confirmed from more recent measurements [8]. Concerning their oxide counterparts, thiogermanates also seem to display a marked optical nonlinearity [15] and represent, therefore, promising materials for the incorporation of rare-earth ions in optical applications [16]. However, photoinduced phenomena that modify the glass structure and properties [17] might limit such possibilities.

Molecular simulations within density functional theory (DFT) appear to be very helpful in decoding the macroscopic behavior or properties and the structure functions that provide only an overall characterization of the system. Efforts in this direction have been only approximate. In a first and detailed attempt to model GeS_2 and sodium thiogermanate glasses from *ab initio* simulations [18–20], Jund and coworkers have used a non-self-consistent DFT scheme building on the Harris functional [21,22] implemented within the local density approximation (LDA). Results which have been refined since then from a more rigorous basis [23] were rather unexpected due to the large number of coordination defects (threefold coordinated sulfur), small amounts of homopolar Ge-Ge bonds found in the glass, including at low Na content [19]. A more recent effort [8] has been using reverse Monte Carlo (RMC) fits to get a structure compatible with x-ray scattering measurements of $50Na_2S$-$50GeS_2$ (NS). The resulting unrelaxed configuration was then used for low temperature (600 K) and extremely short time (5 ps) investigations using DFT simulations to infer a crude description of the ion dynamics.

There is, therefore, much to learn from a more rigorous approach building on the full plane-wave basis as performed for the network former GeS_2 [23,24], in a combination of an enhanced methodology taking into account (i) increased system sizes concerning previous work [19], (ii) improved DFT modeling in the spirit of the results obtained for the network formers [23,24] with a generalized gradient approximation (GGA), and (iii) aspects of relaxation that are not handled at all in certain studies [8] with statistical averages performed within linear response theory to extract transport and electric properties.

We present an extended experimental and theoretical investigation of the Na_2S-GeS_2 glass and liquid system by performing a thorough experimental and theoretical analysis. X-ray scattering indicates a profound alteration of the network structure at elevated Na content that substantially modifies the structure functions in real and reciprocal space. With temperature, the conductivity measurements reveal for Na-containing compositions ionic conduction of Arrhenius type, whereas additional measurements at different temperatures for a much larger number of compositions allow the identification of a power-law increase of σ after a specific low threshold composition $x_c \simeq 1.0\%$, and a nearly smooth increase which differs from previously investigated sulfide electrolytes. The theoretical investigation of GeS_2, Na_2S-$2GeS_2$ (NG2), and $2Na_2S$-GeS_2 (N2G) permits the validation of the DFT model structures from a direct comparison with the x-ray scattering results. The resulting analysis suggests a network that loses its medium-range ordering (ring statistics) and increases the void density by up to nearly 50% at significant Na content. In contrast, the calculated Q^n speciation is similar to the one encountered in corresponding isochemical oxides. Finally, evidence for preferential pathways (channels) is evidenced together with isolated $(Ge_2S_6)^{6\ominus}$ anions that contain homopolar Ge-Ge bonds. Taken together, these results highlight the central role played by network depolymerization that promotes ion conduction, which is found to be as large as 10^{-4} $\Omega^{-1}\,cm^{-1}$.

II. METHODS

A. Glass preparation

The investigated samples were xNa_2S-$(100\text{-}x)GeS_2$ glasses with $x \leqslant 66\%$. Bulk glasses ($x \leqslant 60$) were prepared from high-purity (4 N) elements by the melt-quenching technique. The materials were synthesized by placing the powdered elements in stoichiometric proportions (for a total batch of $\simeq$0.5 g) in a cylindrical quartz ampoule that was evacuated up to a pressure of 10^{-5} mbar and then sealed. The tube was subsequently heated in a furnace with a low heating rate of 10 °C/h up to 950 °C, held at this temperature for eight h, and finally quenched into a mixture of ice and water to obtain the glassy materials.

The ball-milling technique was used to synthesize the $66Na_2S$-$34GeS_2$ glass. Stoichiometric ratios of the Na_2S (Sigma-Aldrich) and GeS_2 (precursor prepared in the laboratory) reagents were intimately mixed in a mortar and pestle and placed in a 20-mL ZrO_2 ball-milling jar along with 80 (diameter = 5 mm) ZrO_2 balls. The batch weighed 3 g, with a ball-to-powder weight ratio of 11/1. The jars were placed in a planetary ball mill (Pulverisette 7 Premium Line, Fritsch) in an argon atmosphere in a glove box to reduce oxidation. The synthesis of this sample was done in three steps. We started at $60Na_2S$-$40GeS_2$ composition, and by addition of Na_2S, we went to $63Na_2S$-$37GeS_2$ and then to $66Na_2S$-$34GeS_2$. 12 rotation cycles of 3 h (36 h of milling) at 510 rpm were scheduled with break and milling the block between each cycle. After every two cycles, a small amount of the powder (0.1 g) has been taken out for x-ray diffraction (XRD) analysis.

B. X-ray diffraction

The experimental structure factors $S(k)$ and the atomic pair distribution function $g(r)$ of these archetypal glassy electrolytes are investigated from x-ray total scattering (XRD). Measurements were performed at room temperature with a dedicated laboratory setup based on a Bruker D8 advance diffractometer ($\lambda = 0.709\,318$ Å) equipped with a molybdenum sealed tube and a rapid LynxEye XE-T detector. This setup was modified to maximize collected intensities, minimize spurious signals from the empty environment, and obtain good counting statistics up to a large scattering vector length of $k_{\max} = 17.2$ Å^{-1}. For each sample, a small amount of powder was placed in a thin-walled (0.01-mm) borosilicate glass capillary of sufficiently small diameter (about 0.5 mm) to limit the absorption effects. The μR values (R being the radius of the capillary and μ the linear attenuation coefficient of the sample) were estimated, using precise measurements of the mass and dimensions of the samples, to be 0.80, 0.85, and 0.65 for GeS_2, NG2, and N2G, respectively. Once sealed, the capillary was mounted on a goniometric head and adjusted so that its axis coincides with the goniometer axis of the diffractometer. The data acquisition consisted of several scans in the 0°–152°, 50°–152°, and 100°–152° ranges with a step size of 0.01°. The scans were subsequently merged, leading to a total equivalent acquisition time of about 120 h per sample. Raw data were corrected, normalized, and Fourier transformed using a homemade software [25] to obtain the sample's atomic pair distribution function $g(r)$. The corrections included capillary, empty environment, Compton and multiple scatterings, absorption, and polarization effects. The x-ray mass attenuation coefficients, atomic scattering factors, and Compton scattering functions needed for data correction and normalization were calculated from tabulated data provided by the DABAX database [26]. The absorption correction was evaluated using a numerical midpoint integration method where the cross section of the sample is divided into a set of small subdomains following a method similar to that proposed by Soper and Egelstaf [27]. The normalization constant was determined using the high-angle method so that the coherently scattered intensity oscillates weakly around the sample's average atomic scattering factor at high values of the scattering vector length (from $k_{\max}/2$ to $k_{\max}$).

C. Conductivity

The ionic conductivity of the $x\mathrm{Na_2S}$-(100-x)$\mathrm{GeS_2}$ glasses was determined by complex impedance spectroscopy (CIS). The pellets of chalcogenide glasses (10 mm in diameter) were obtained by applying a force of 2.5 tons for 25 min. Then, the platinum electrodes were sputtered on their parallel opposite faces to ensure electrical contact. Electrical measurements were conducted using a Solartron SI-1260 impedance analyzer over the frequency range 10 MHz–10 Hz, with an applied root-mean-square AC voltage of 500 mV. These measurements were carried out under primary vacuum, at temperatures below the glass transition temperature T_g in the range 300–433 K.

Electrical conductivity data are obtained from complex impedance spectroscopy analysis. Resistances (R) of the samples are taken from the intercept of the impedance response with the real axes at low frequency, and the DC conductivity is calculated according to the relationship $\sigma_{\mathrm{DC}} = e/RA$, where e is the thickness and A is the area of the sample.

D. Molecular dynamics

First-principles molecular dynamics (FPMD) simulations (Car-Parrinello scheme [28]) have been performed on the three compositions GeS_2, NG2, and N2G within a canonical (NVT) ensemble using the same DFT simulation scheme described below. For the Na-containing systems, the simulation box contains $N = 300$ atoms with the number of Ge, S, and Na atoms fulfilling the desired stoichiometry, i.e., $N_{\mathrm{Ge}} = N_{\mathrm{Na}} = 66$ and $N_{\mathrm{S}} = 168$ for NG2 (Fig. 1). The simulation box of GeS_2 contained $N = 120$ atoms, and structure results have been extensively discussed in Ref. [24]. In the forthcoming, we use only the appropriate XRD weighted structure functions directly compared to our measurements. A periodically repeated cubic cell was used, with edges L satisfying the experimental number density of the corresponding glasses [3,29], e.g., $L = 19.26$ Å for N2G. We used DFT in combination with plane-wave basis sets, the electronic scheme being based on a BLYP functional [30,31] within GGA for the exchange-correlation energy. The choice of this functional is motivated by the fact that previous investigations of base networks have led to a very accurate structural description of amorphous state [32–35] and especially GeS_2 [23,24]. The electronic structure of the liquids and glasses was described within DFT and evolved self-consistently during the motion, with valence electrons being treated explicitly in conjunction with norm-conserving pseudopotentials to account for core-valence interactions. The wave functions were expanded at the Γ point of the supercell and the energy cutoff was set at 80 Ry.

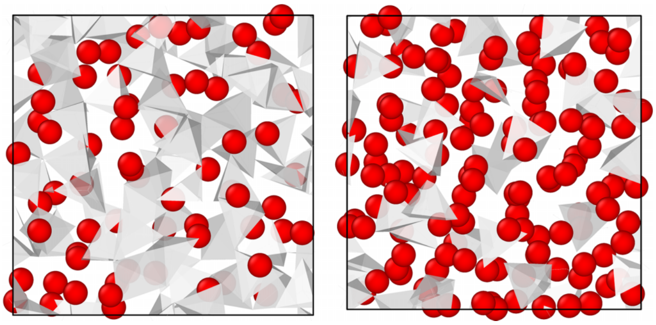

FIG. 1. Typical snapshots at 300 K of the investigated 300 atomic amorphous $x\mathrm{Na_2S}$-(100-x)$\mathrm{GeS_2}$: $x = 33\%$ (NG2, left) and 66% (N2G, right). Na atoms are represented in red, and Ge tetrahedra are light gray.

The starting configurations of the Na-containing glasses were a random distribution of Ge, S, and Na atoms. Loss of memory of the initial configurations has been achieved through preliminary runs at 2000 K over 20 ps with a time step of $\Delta t = 0.12$ fs and a fictitious mass of 2000 a.u., before different equilibrations at 1500, 1200, 900, and 600 K, each accumulated at 20–30 ps, and finally 300 K for 30 ps. The cooling procedure was performed sequentially, e.g., the equilibration at 900 K started from the last configuration (positions/velocities) obtained at 1200 K, and so on. The presented results at 300 K are obtained from a statistical average over 25 ps once the first 5 ps have been discarded. As in the isochemical sodium silicate structure, the resulting model structure reveals a network made of tetrahedra (here $\mathrm{GeS_{4/2}}$) that is disrupted by the Na ions (Fig. 1).

To characterize the bonding and localization properties of the modified thiogermanates, we used the formalism of the Boys localized orbitals [36,37] which are calculated as their periodic system generalization, corresponding to maximally localized Wannier functions (MLWF) $w_n(\mathbf{r})$:

$$w_n(\mathbf{r}) = \sum_{m=1}^{J} U_{mn}|\Phi_m\rangle \qquad (1)$$

and provide an efficient way [38–40] to represent the electronic distribution around atoms in various materials [41–43]. From the Kohn-Sham states Φ_m, the unitary matrix U_{nm} associated with the Bloch orbitals is determined by an iterative minimization of the Wannier function spread Ω in real space :

$$\Omega = -\frac{1}{(2\pi)^2} c_\alpha \ln|\langle\Phi_m|e^{i\mathbf{G}.\boldsymbol{r}}|\Phi_m\rangle|^2, \qquad (2)$$

where c_α are weights assigned to each x, y, z axis, and $G_\alpha = 2\pi/L$. The corresponding MLWF centers can then be computed:

$$\bar{\mathbf{r}}_n^w = -\frac{L}{2\pi}\mathrm{Im}[\ln\langle w_n|e^{i\mathbf{G}.\boldsymbol{r}}|w_n\rangle]. \qquad (3)$$

These serve below to characterize the nature of the chemical bonding of thiogermanates.

III. RESULTS AND DISCUSSION

A. Comparison of structure functions

Figure 2(a) displays the calculated and measured x-ray structure factor, where the former has been calculated using an x-ray weighted sum of partial correlations $S_{nm}(k)$ in Fourier space:

$$S(k) = \langle f\rangle^{-2}\sum_{n,m} c_n c_m f_n f_m S_{nm}(k) \qquad (4)$$

with

$$\langle f\rangle = \sum_n c_n f_n = (1-x)f_{\mathrm{Ge}} + 2x f_{\mathrm{Na}} + (2-x)f_{\mathrm{S}}, \qquad (5)$$

where the f_n and c_n represent the atomic form factors taken as $f_n = Z_n$ ($f_{\mathrm{Ge}} = 32$, $f_{\mathrm{S}} = 16$, $f_{\mathrm{Na}} = 11$) and species concentration, respectively. A k dependence of the form factors did not lead to significant differences. The partial correlations have been evaluated from a Fourier transform of the partial pair correlation functions $g_{nm}(r)$:

$$S_{nm}(k) = 1 + \rho_0\int 4\pi r^2[g_{nm}(r) - 1]\frac{\sin(kr)}{kr}dr, \qquad (6)$$

where ρ_0 is the system number density accessed from the experiment [3,29].

For the three compositions, the comparison between the calculated $S(k)$ [red curves, Fig. 2(a)] reproduces rather well the present measured XRD total structure factor (black) which are also consistent with previously XRD measured data for NG2 [7] and $\mathrm{GeS_2}$ [29] as all peaks are nearly reproduced in position, amplitude, and width, except in the low-k region of the NG2 composition where the simulation overestimates the position of the first sharp diffraction peak observed at $k_1 = 1.05$ Å^{-1}. For NG2 and N2G, the diffraction pattern is dominated by three peaks found at $k_1 = k_{\mathrm{FSDP}} = 1.05$ Å^{-1}, $k_2 \simeq 2.16$, Å^{-1}, and $k_3 \simeq 3.68$ Å^{-1}, a feature also observed for another composition (NG [8]). The increase of Na content induces a progressive decrease of both the peak amplitude at k_2 and k_3 so that the contrast $S(k) \neq 1$ is significantly reduced for N2G, this situation being found in simulation and experiments. A comparison with the data of $\mathrm{GeS_2}$ [Fig. 2(a)] shows that the structure of NG2 is still close to the one of the base network former, as the general profile is similar with not only the pattern of the two principal peaks and the FSDP being close, but also the one found at 6–7 Å^{-1} and $\simeq 9$ Å^{-1}. This result is probably anticipated because NG2 is weakly depolymerized and Na-based correlations do not contribute substantially to the total $S(k)$.

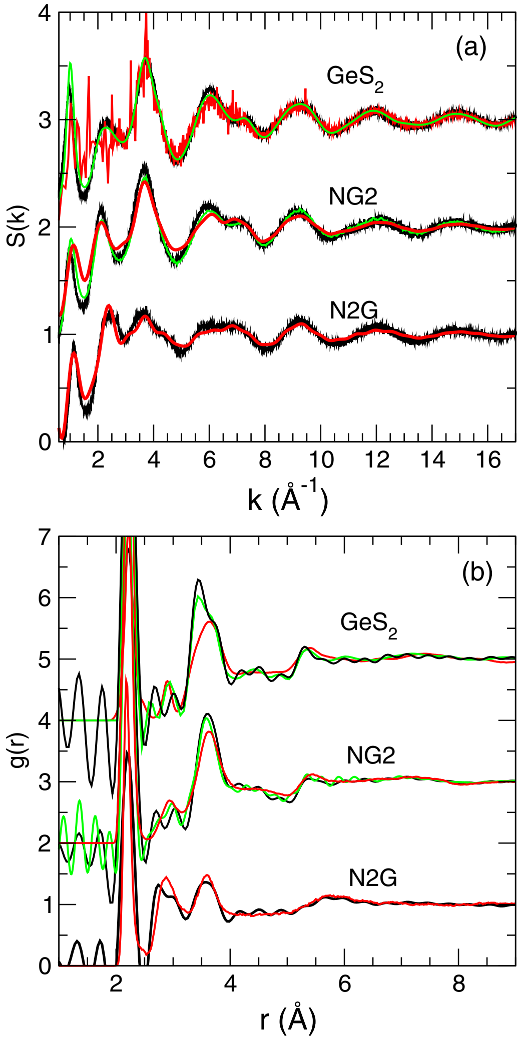

FIG. 2. Calculated (red) and measured (black) total structure factor $S(k)$ (a) and pair correlation functions $g(r)$ (b) for $\mathrm{GeS_2}$, NG2, and N2G glasses. In addition, XRD data from Itoh *et al.* [7] (NG2 composition, green) and Zeidler *et al.* [29] ($\mathrm{GeS_2}$ composition, green) have been added.

We, furthermore, note that the peaks beyond the principal peak regions are correctly reproduced. A Gaussian decomposition of $S(k)$ has shown that such peaks ($k \simeq$ 6–7 Å^{-1}) result from well-defined second-neighbor correlations [44]. As the double-peak distribution in this region tends to vanish with increasing Na content, it is tempting to relate this feature with the increase in the Na-related loose neighborhood.

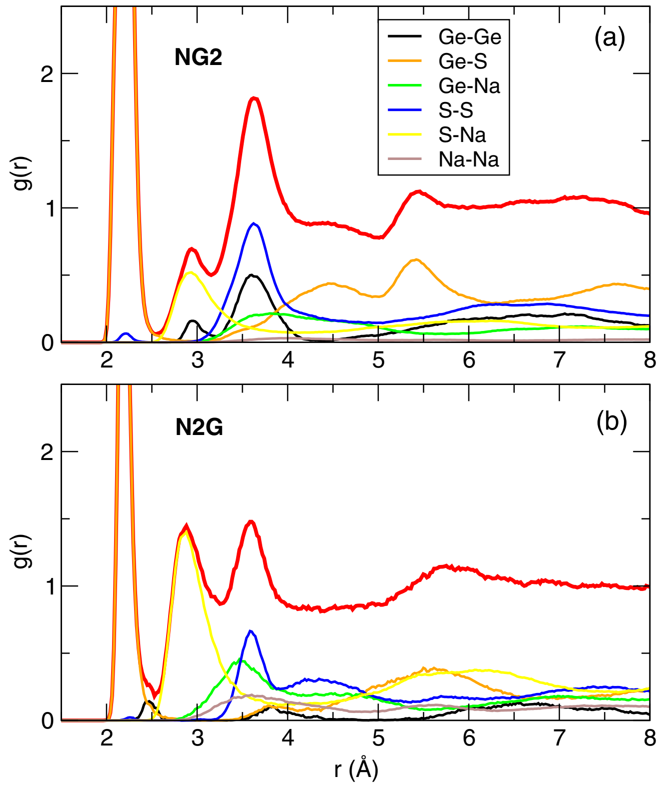

FIG. 3. Decomposition of the calculated pair correlation function (red curves, same as Fig. 2) of NG2 (a) and N2G (b) into weighted partials.

B. Real-space properties

Real-space properties are represented in Fig. 2(b) with the calculated and x-ray measured pair correlation function $g(r)$, together with similar experimental results [29] for GeS$_2$ and NG2 [45]. We note that the main features are reproduced with excellent accuracy from the simulation for all compositions, that is, positions and amplitudes of the 2–3 principal peaks at $r_1 \simeq 2.20$ Å and $r_2 \simeq 3.65$ Å as well an intermediate peak at $r_3 \simeq 2.90$ Å whose intensity grows with Na content. The nature of this peak is, indeed, evolving with Na content. In the base glass, this peak is associated with the presence of edge-sharing tetrahedra [24]. As depolymerization occurs, the third peak is progressively linked with the growing presence of Na-S correlations, which appear to become dominant at significant Na content (N2G).

An inspection of the weighted partials $\langle f \rangle^{-2} f_i f_j c_i c_j g_{ij}(r)$ permits to analyze in detail the origin of the measured features of the total $g(r)$ (Fig. 3). While the base geometry will remain tetrahedral (see below), which induces intense peaks at the relevant Ge-S (apex of the tetrahedra, $r_1 = 2.35$ Å) and S-S (edge of the tetrahedra, $r_2 = 3.65$ Å), the other correlating distances will substantially depend on composition. At low Na content (NG2), the network remains dominated by corner- and edge-sharing connections, which respectively lead to typical Ge-Ge distances that contribute to the peak at r_2 (CS tetrahedra) and, to a much lesser extent, to the height at 2.94 Å [Ge-Ge correlations arising from ES tetrahedra as in the base GeS$_2$ [24], see also Fig. 4(a) below]. An additional contribution arises from the sodium environment contributing to NBS-Na correlations at nearly the same

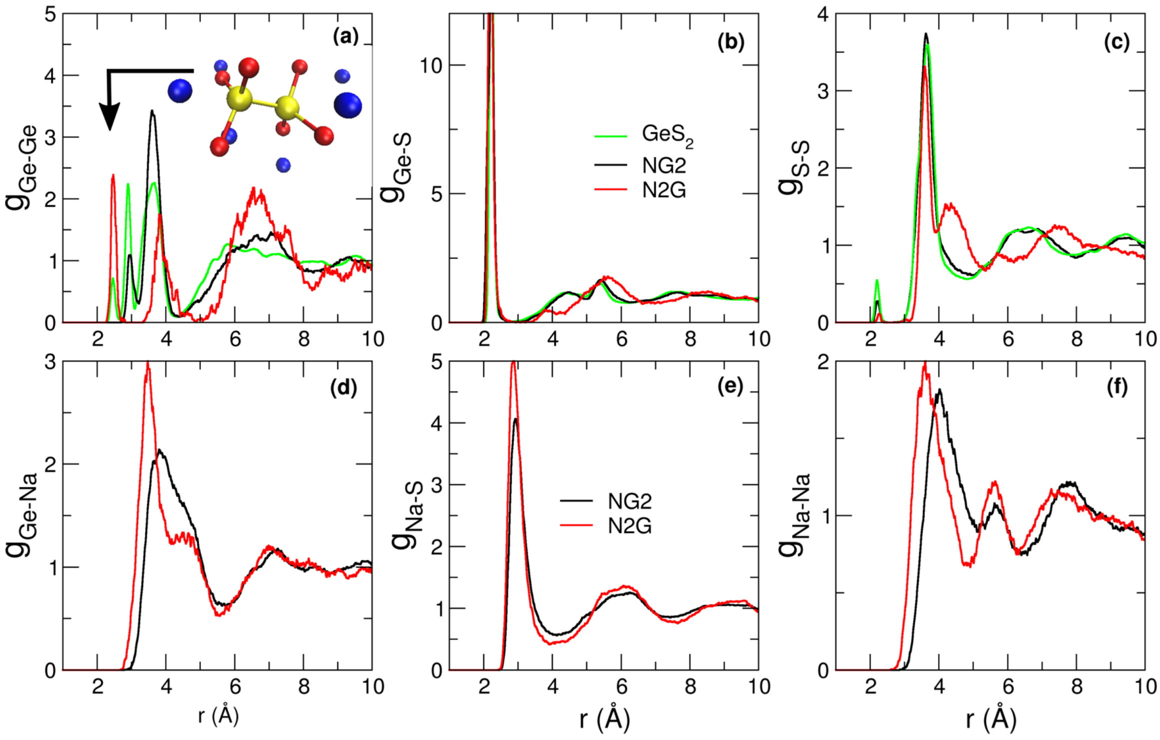

FIG. 4. Partial pair correlation functions $g_{ij}(r)$ of NG2 (black) and N2G (red), together with corresponding partials for amorphous GeS$_2$ (green [24]). In (a) is represented a Ge$_2$S$_6^{6\ominus}$ that leads to a typical Ge-Ge homopolar bond. Ge, S, and Na atoms are colored in yellow, red, and blue, respectively.

distance (yellow curves in Fig. 3, 2.94 Å). With increasing Na content [Fig. 3(b)], such correlations now grow markedly and mostly contribute to this intermediate peak with an intensity comparable to the one measured at r_2. Additional correlations now emerge, such as Na-Ge and Na-Na, which directly also contribute to the peak at r_2. These changes, thus, underscore a dramatic alteration of the base GeS_2 network that is depolymerized by alkali addition.

1. Partial correlations

Additional insight is provided from Fig. 4, which represents the partial pair correlations (unweighted in contrast to Fig. 3) for the three systems of interest. The GeS_2 glass exhibits three distinct peaks in the $g_{\text{Ge-Ge}}(r)$ function [Fig. 4(a)], which reflects, as previously mentioned, the presence of homopolar Ge-Ge bonds at the shortest distance (2.46 Å), edge sharing (at 2.92 Å), and corner sharing (at 3.89 Å), respectively. These features are unambiguously identified from the isochemical $GeSe_2$ for which full resolution of the partials using isotopic substitution in neutron diffraction has been achieved [46]. Although one cannot entirely rule out a possible effect due to thermal history [47], homopolar Ge-Ge bonds are specific to thiogermanates and not seen in corresponding oxides. It is probably also important to emphasize that such chemical defects might only result from typical base network features. Silicon oxides and chalcogenides do not exhibit at all homopolar bonds and, as a result, one does not detect them in corresponding modified systems such as silicates [48] or thiosilicates [49]. Conversely, since such defects exist in GeS_2 [24,29] and $GeSe_2$ [33], one might expect that thiogermanates and seleniogermanates such as Na_2Se-$GeSe_2$ exhibit them at select compositions, as also discussed below. The ES-sharing distance disappears for the glass containing 66% Na_2S, which is independently confirmed by the ring analysis (Sec. III B 5).

The second main outcome is the fact that pair correlation functions involving the network-forming species [Figs. 4(b) and 4(c)] display a moderate evolution with Na content, which reflects that the typical short distances defining the tetrahedra are maintained, i.e., the Ge-S (2.20 Å) and the S-S distances (3.60 Å). Conversely, for such partials, the evolution with Na content indicates that second-order correlations are modified, e.g., 4.48 Å in NG2 to 5.60 Å in N2G [Fig. 4(b)], and these are induced by the growing presence of Na-rich subregions [see snapshot Fig. 1(b)], as also reflected by the emergence of a typical S-S distance [4.43 Å in Fig. 4(c)] that is linked with the growing presence of NBS atoms. One, furthermore, notes that chemical bonding defects reduce with increasing Na content, i.e., the intensity of the typical S-S homopolar peak observed [24,29] in GeS_2 at 2.23 Å progressively vanishes upon Na addition. Finally, the reduction of the specific correlating distance Na-Na for N2G [Fig. 4(f)] reflects the growing presence of Na ions and the effect of their heterogeneous distribution, which also manifests in reciprocal space at the intermediate range.

2. BS versus NBS distances

It is known that silicates display a marked difference in the Si-O bond length, depending on whether the oxygen atoms are connecting two Si tetrahedra (a BO atom analogous to the present BS atom) or being involved in the vicinity of a Na ion (nonbridging oxygen, NBO). These features are observed in crystalline silicates [50,51] and have also been quantified in simulated glasses [52–54]. In the latter, the bond distance difference is about 0.08–0.1 Å, i.e., the Si-BO bond length is slightly longer than the Si-NBO one. For the specific case of sodium silicates [53] the difference is of about 0.1 Å although such differences continue to be discussed both from experiments and simulations [48,55,56]. Recently, it has been shown that in thiosilicates such differences were also detected [49] albeit with a much smaller difference (0.03 Å). Therefore, one might wonder if the same features are also found in thiogermanates.

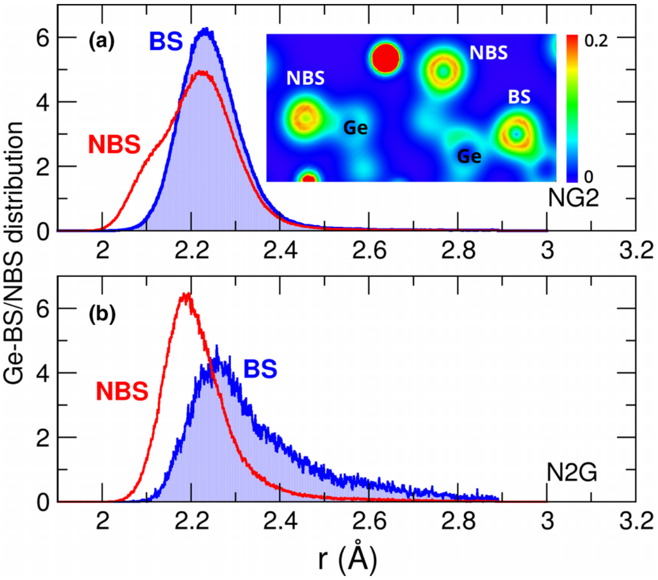

FIG. 5. (a) Calculated distribution of Ge-BS (blue) and Ge-NBS bonding (red) distances for N2G and NG2 glasses. The electronic densities (atomic units) in a slice (thickness 0.2 Å) around BS and NBS atoms are represented in (a). Red-colored electronic densities are associated with the Na ions.

Figure 5 represents the calculated Ge-BS and Ge-NBS bond-distance distributions. As in thiosilicates [49] or alkali silicates [52–54], we also find a bond-length difference in both NG2 and N2G that is equal to 0.01 and 0.08 Å, respectively (Fig. 5). We note that, in general, the group IV-BS/NBS bond-length difference appears to be smaller (see also results on lithium thiosilicates [49]) when compared to corresponding oxides, i.e., silicates or germanates. This feature is evident for the weakly modified GeS_2 (NG2), for which the maximum of both distributions nearly coincides at 2.23 Å.

An additional feature for the NG2 glass consists of a marked shoulder on the low-r side of the Ge-NBS distribution at $r \simeq 2.1$ Å [Fig. 5(a)]. A visual inspection of the atomic snapshots with their Ge-NBS distances indicates that such shorter distances are systematically found on Q^n ($n < 4$) tetrahedra which are part of an ES motif (distance marked in red in Fig. 6) in E^k ($1 \leqslant k \leqslant 2$) configurations where k denotes the number of edges shared by a tetrahedron [14]. This identification is, furthermore, consistent with the fact that this shoulder contribution is not found for the N2G composition where ES motifs are absent [Fig. 4(a)], as also acknowledged from the

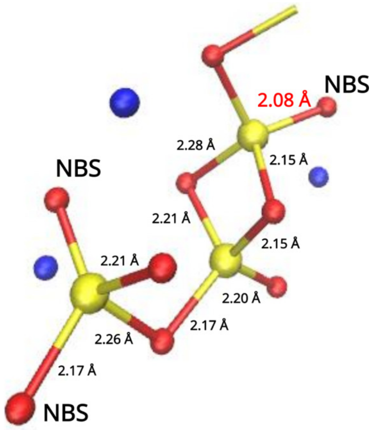

FIG. 6. Snapshot of an atomic fragment of the NG2 glass network showing typical Ge-BS and Ge-NBS distances involved. The Ge-NBS distances, which are part of an ES (E^2 or E^1 tetrahedra) structure, are systematically lower (in red) and contribute to the shoulder contribution at $r \simeq 2.01$ Å in the Ge-NBS bond distance distribution [Fig. 5(a)]. Ge, S, and Na atoms are represented in yellow, red, and blue, respectively.

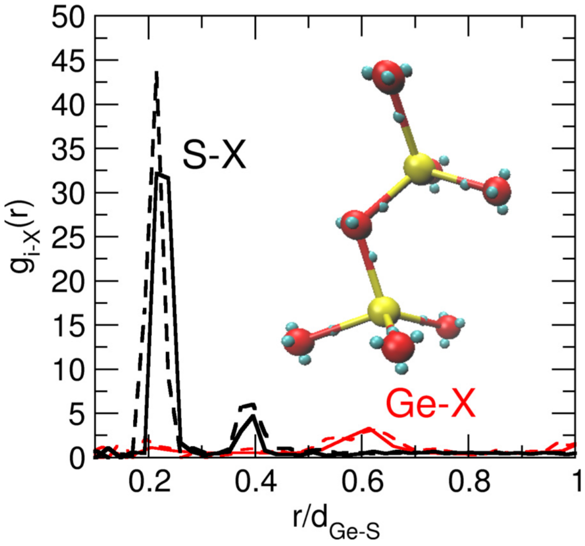

FIG. 7. Calculated atom-MLWF center correlations for NG2 (broken lines) and N2G (solid lines) as a function of the rescaled distance $r/d_{\text{Ge-S}}$. The snapshot represents the location of the MLWF centers (blue spheres) on a typical Q^1-Q^1 dimer.

ring statistics discussed below. Conversely, E^0 motifs (i.e., no edge sharing) lead to Ge-NBS distances that contribute to the main peak at 2.23 Å [Fig. 5(a)]. Here, and although such differences are found to be smaller as compared to oxides, one still observes a difference for N2G that mimics the one encountered in silicates or thiosilicates, i.e., the Ge-NBS distance is slightly shorter (2.19 Å) than the Ge-BS distance (2.25 Å). The physical origin of this bond distance difference is common to silicates and thiosilicates. It is linked with the influence of the alkali ions on the neighboring charges and the Ge-NBS ion-covalent character of the bonding that modifies the electronic structure of the next-neighbor germanium atoms. The effect is weaker in sulfide glasses because the electronegativity difference with Na is smaller [57] ($\Delta\chi_{\text{Na-S}} = 1.51$ and $\Delta\chi_{\text{Na-O}} = 2.37$). One thus expects to see charge separation (i.e., ionic character) reduced with a possible reduced alteration of the Ge environment. With the small amount of Na ions in NG2, its, therefore, not surprising that such a bond distance difference is smaller.

Such a moderate electronegativity difference between the atoms reflects a delicate balance between electron localization on the atomic sites involved in ionic bonding and electronic delocalization, i.e., covalent effects. An inspection of the nature of the chemical bonding via the DFT calculated spatial distribution of the electronic density reveals several features that might be responsible for this bond-length difference. Because of the nondirectional character of the NBS-Na bond, the electronic density of NBS atoms points essentially towards the close Ge atom with a relatively well-defined depletion of the valence charge [contour plot in Fig. 5(a)] with the (positive) electronic density very well localized on the Na ions (red). This feature contrasts with the characteristics obtained for the BS atoms. The p orbitals contribute to the deformation of the valence charge in a direction perpendicular to the Ge-Ge line connecting two CS tetrahedra and involves a reduced depletion (see contour plot).

The second probe regarding BS and NBS differences arises from the MLWF centers, which capture electronic localization properties, and the location of such centers (snapshot in Fig. 7) now also indicates the presence of an apparent link between electronic charge location and the bonding or nonbonding nature of the sulfur atom. Because of a Na atom in its vicinity, charge separation on NBS atoms involves an s-type MLWF, which corresponds to a lone pair. In contrast, other MLWFs are found along the Ge-S bonds and correspond to localized p-type centers involved in the covalent bond. The number of such MLWF centers differs depending on the nature of the sulfur atom, BS or NBS, as one finds two and three MLWFs, respectively. These features are visible once species-dependent (Ge, S) correlation functions with MLWF centers $g_{i-X}(r)$ ($i =$ Ge, S) are represented (Fig. 7). For the sulfur atoms, one acknowledges a dominant peak at $r \simeq 0.2 d_{\text{Ge-S}}$ which corresponds to the apparent presence of the nonbonding (lone pair) electrons. Both species then display peaks at distances of about half the typical Ge-S bond length (Fig. 7). This can be rationalized by invoking the larger electronegativity of the S atoms and the resulting electron charge transfer occurring toward the S atoms, leading to a peak at $r < d_{\text{Ge-S}}/2$. In contrast, the opposite behavior is acknowledged for the Ge atoms ($r > d_{\text{Ge-S}}/2$).

As BS and NBS are identified on, e.g., the N2G compound, the corresponding BS-X and NBS-X pair correlation functions reveal some additional features and indicate a different electronic structure for the sulfur atoms. While $g_{\text{BS-}X}$ has an amplitude at $r \simeq 0.48$ Å ($r/d_{\text{Ge-S}} \simeq 0.22$) that is larger than the one of $g_{\text{NBS-}X}$ which is consistent with the fact that there are more MLWF centers around NBS atoms (snapshot Fig. 7), BS atoms have a specific short-range correlation detected at $r \simeq 0.27$ Å (barely seen in Fig. 7). Such subtle differences in electronic bonding properties might be responsible for the obtained and observed bond-length differences in silicates, thiosilicates and the present thiogermanates [49,52–54].

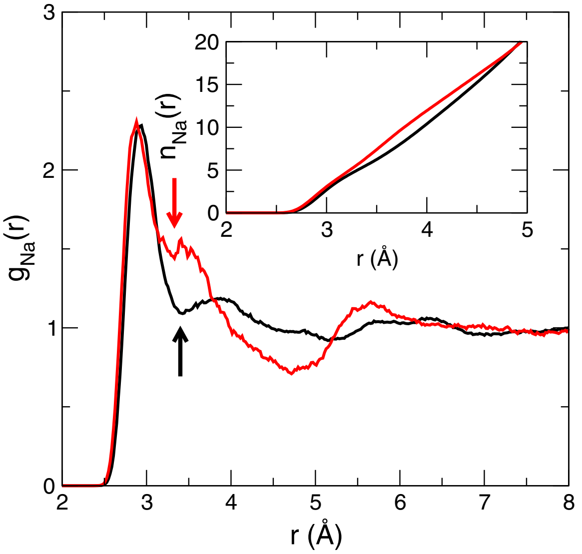

FIG. 8. Calculated Na pair correlation function for NG2 (black) and N2G (red). The inset shows the running coordination number $n_{Na}(r)$. Arrows indicate the location of r_{min}.

3. Coordinations and Q^n speciation

Using the pair correlation functions $g_{ij}(r)$ (Fig. 4 and the number densities ρ_0 [3,29]), we evaluate the total coordination numbers $n_i(r)$ defined by

$$n_i = 4\pi\rho_0 \int_{r_0}^{r_{min}} r^2 g_i(r) dr, \quad (7)$$

the lower integration bound r_0 being fixed to 1.9 Å for all compositions, and the upper bound r_{min} values chosen as the value of the first minimum r_{min} of each $g_i(r)$ function that represents the species weighted correlation function $g_i(r)$ (i = Ge,S, Na), e.g., $r_{min} \simeq 3.40$ Å for g_{Na} (Fig. 8). For the Ge coordination, we find 3.98 and 3.84 for NG2 and N2G, which is compatible with the obvious tetrahedral character of the network and also extended x-ray absorption fine structure (EXAFS) measurements [6], whereas $n_S = 1.90$ for both compositions. The Na coordination number is less well defined as evidenced by the corresponding coordination number function $n(r)$ (inset of Fig. 8), which does not display a plateau behavior (as for Ge or S) resulting from the condition $g(r_{min}) \rightarrow 0$. For NG2, we find $n_{Na} = 5.63$, and for the high Na content, obvious additional contributions (Na-Na) lead to a poor separation of the first and second shell of neighbors but using $r_{min} = 3.33$ Å we obtain $n_{Na} = 5.82$. This estimate reflects that the Na subnetwork of highly depolymerized glasses has a loose structuration with features in correlations typical of high-temperature liquids.

As mentioned above, a convenient means to analyze the short-range order uses the notion of Q^n speciation where n represents the number of BS atoms as first neighbors of a central Ge atom. Table I displays the calculated population for the Na-containing compositions of interest. At low Na content (NG2), the structure contains a dominant population of Q^3 and Q^2 species. A certain depolymerization is acknowledged that manifests by the weak population of Q^4 species typical of the base GeS_2 network (7.2%), and much smaller than the one found in corresponding silicates NS2 [59,60], i.e., 26.6%–35.9%. In any case, these Q^n populations appear not to follow what would be expected from an ideal chemical model having 100% Q^3 and 100% Q^0 for NG2 and N2G, respectively, or from a random model [58]. Here, the apparent increased depolymerization that manifests by an increased fraction of Q^2, Q^1, and Q^0 species concerning alkali silicates might be one of the structural reasons for the increased conductivity in sulfide glasses.

TABLE I. Calculated fraction of Q^n distribution (in %) in NG2 and N2G glasses, and compared to various models from the literature including sodium silicates (NS2 [59,60]).

	Q^4	Q^3	Q^2	Q^1	Q^0
NG2	7.2	34.7	30.2	23.1	4.9
Ideal chemical NG2 model	–	100.0	–	–	–
Random NG2 model [58]	37.9	41.4	16.7	3.0	–
NS2 (^{29}Si NMR) [59]	26.6	68.4	4.8	–	–
NS2 (MD) [60]	35.9	44.1	18.6	1.3	–
N2G	–	–	–	41.1	58.9
Ideal chemical N2G model	–	–	–	–	100.0

Interestingly, for the Na-rich glass one detects homopolar Ge-Ge bonds in the structure [Fig. 4(a)], and these are typical of chalcogenide networks such as $GeSe_2$ [33], GeS_2 [29], or ternary Ge-As-Se [61]. Their presence alters the definition of Q^n species (assumed to be 100% heteropolar in oxides with 100% Si-O bonds for any n). Our statistical analysis reveals that 30% of the identified Q^1 units in N2G (41.1%, see Table I) contain a Ge-Ge homopolar bond, and define a $(Ge_2S_6)^{4\ominus}$ anion [see snapshot Fig. 4(a)]. Such homopolar anions have also been detected in the parent thiophosphate system [62] where the presence of $(P_2S_6)^{4\ominus}$ anions involving a P-P homopolar bond is supposed to promote ionic conduction.

4. Bond angles

Figure 9 now represents the relevant bond-angle distributions (BAD) for both compositions, which are also compared to results [24] for Ge-S-Ge and S-Ge-S of amorphous GeS_2 (green curves).

Interestingly, the NG2 compositions display a bimodal distribution for the Ge-S-Ge BAD [Fig. 9(a)] that indicates the presence of both CS- and ES-sharing tetrahedra, the peak at ≃80° being associated with the latter. In contrast, the main peak at ≃105° is the signature of BS atoms linking the Ge tetrahedra by corners. This distribution and the S-Ge-S one [Fig. 9(b)] are found to be very close to the BADs obtained for the network former (green curves [24]), which signals that the average topology of the underlying network has not been substantially modified by the Na ions. Indeed, it predominantly consists of a connection of $GeS_{4/2}$ tetrahedra as detected from the dominant peak found at $\theta_T = \arccos(-\frac{1}{3}) = 109.47°$. However, we also note the presence of a shoulder peak in GeS_2 [Fig. 9(b)] at ≃95° that is still visible for NG2 but absent in the NG2 glass. This contribution arises from the presence of ES motifs, which contain the S-Ge-S bond angle and lead to an obvious reduction from θ_T. The important addition of Na ions (red curves) induces a rather

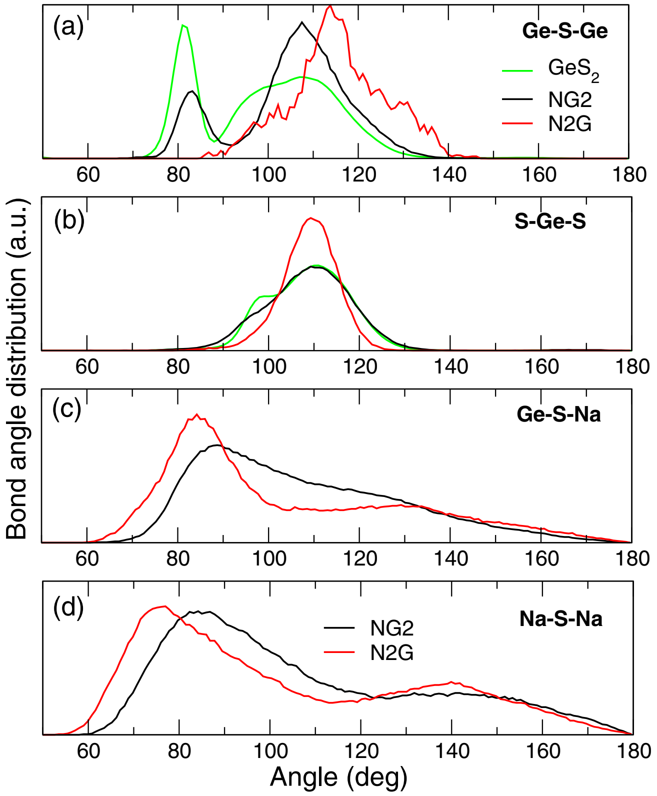

FIG. 9. Normalized bond-angle distributions of NG2 (black) and N2G (red). Some reference BADs (Ge-S-Ge and S-Ge-S) are given for amorphous GeS$_2$ [24] (green).

dramatic evolution of the Ge-S-Ge BAD, whose average angle shifts to larger values (average 112°), in contrast to S-Ge-S whose average angle remains nearly unchanged and centered at θ_T, albeit the BAD profile displays some moderate changes with composition, as described above. This highlights that the tetrahedral character of the Ge atoms is maintained even in the highly depolymerized N2G glass. While Ge-S-Na leads to broad distributions for both compositions [Fig. 9(c)], which suggests the variety of environments found for Na atoms in the vicinity of NBS atoms, the S-Na-S BAD can be analyzed depending on the nature of the sulfur atoms, BS or NBS. Figure 10(a) shows the different possible angles that highlight the possibility for Na to be in a near octahedral environment given the BAD NBS-Na-NBS profile, which has a broad peak centered at $\simeq 90^\circ$ together with a substantial contribution at 180°. This result matches the Na coordination numbers ($n_{\mathrm{Na}} \simeq$ 5–6). These features appear to be close for both compositions, and a slight shift to smaller angles ($\simeq 75^\circ$) is acknowledged for the Na-poor composition (NG2). We note that there is no fundamental difference with the other BAD NBS-Na-BS. The further possible distribution [BS-Na-BS, Fig. 10(b)] appears to be more sensitive to composition, and this arises from the fact that at high Na content, the BS-Na-BS angle can only be detected from two connected Q^1 units.

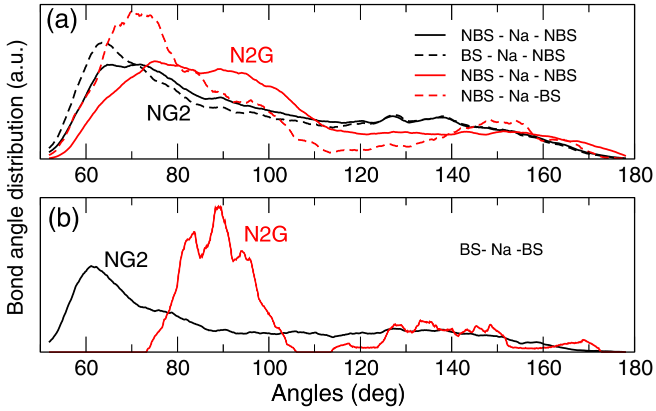

FIG. 10. Normalized bond-angle distributions of NG2 (black) and N2G (red) for NBS-Na-NBS and NBS-Na-BS (a) and BS-Na-BS (b).

5. *Rings and voids*

We have mentioned earlier that the partial pair correlation functions and the total calculated or measured $g(r)$ of the base network GeS$_2$ contain ES tetrahedra representing a $n = 4$ ring. It is instructive to characterize how such medium-range elements and other rings behave with the above-mentioned progressive depolymerization of the network. In the related thiosilicates, such ES fragments have a specific nuclear magnetic resonance (NMR) signature [14] that have been analyzed with composition.

Using a ring-statistics algorithm that builds on a rigorous investigation of networks generated using simulation (RINGS) code [63], we have determined from the simulated structures the concentration of rings of size $n \leqslant 10$ (Fig. 11). Note that the used cutoff (2.80 Å) permits one to focus only on rings belonging to the network species (Ge, S). The algorithm is mainly based on the King [64]-Franzblau [65] shortest-path search to find rings. The statistics over the (Ge, S) network indicates complete depolymerization of the base network upon important Na addition. The base network is dominated in GeS$_2$ by ES and $n = 5$ and six-membered rings

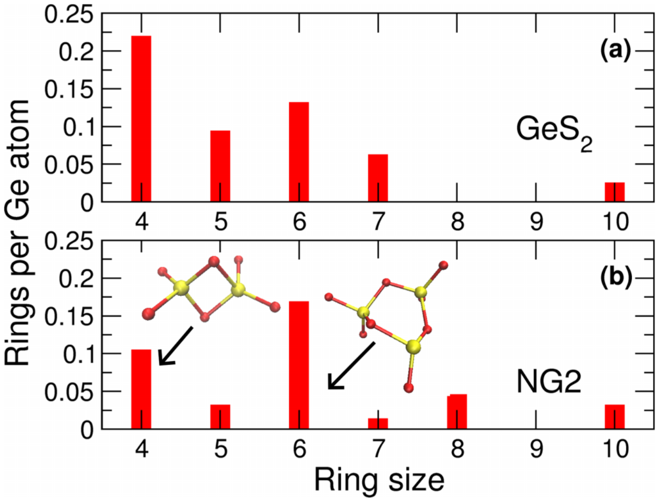

FIG. 11. Calculated ring fraction in GeS$_2$ [24] (a) and NG2 (b). Corresponding ring fragments are displayed with Ge and S atoms colored yellow and red, respectively. A cutoff distance of 2.80 Å has been used to calculate the ring statistics.

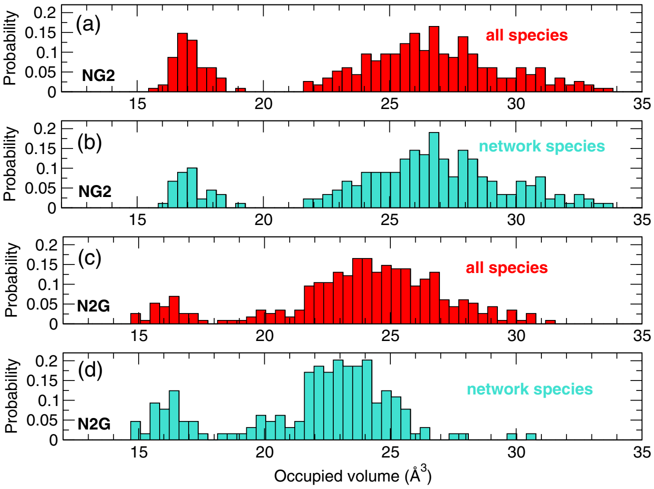

FIG. 12. Occupied volume distribution in NG2 [(a),(b)] and N2G [(c),(d)]. From the full distribution, the contributions arising from the network species (Ge, S) are extracted and appropriately normalized [(b),(d)].

[24] [Fig. 11(a)], which is nearly consistent with the picture of the outrigger raft model made of such elementary building blocks [66] and proposed based on the structure [67] of the crystalline compound (see discussion [68–70]). Here, the computed ring ratio for $n = 4$, 5, and 6 rings is 1:5:5, i.e., somewhat different from the one proposed in the outrigger raft structure, which is 1:2:2 (specifically Fig. 2 in Ref. [66]). Note that the base glass also contains odd-sized rings resulting from homopolar Ge-Ge and S-S bonds, as detected from the corresponding pair correlation functions [Figs. 4(a) and 4(c)].

Adding Na to the base network now modifies the medium-range order rather substantially. At moderate content [NG2, Fig. 11(b)], the structure still retains ES and $n = 6$ membered rings, but the reduction of odd-sized rings ($n = 5$ and 7) is visible and is linked with the obvious reduction of homopolar defects. At larger content (N2G), we note a complete absence of rings. Thus, one can conclude that adding Na into the base network depolymerizes the GeS$_2$ structure and annihilates the covalent network medium range order characterized by the ring structures. Given the Q^n speciation provided above, the remaining (Ge, S) structure will be made only of a small fragments of CS tetrahedra (Q^1-Q^1 dimers) at large Na content.

The inspection of occupied volume within a Voronoi tesselation by the atoms provides an additional way of analyzing the alteration of the network. For each particle [either all species or only the network-related ones (Ge, S)], a Voronoi cell can be defined from the region of space closer to a given atom than any other particle. This is mathematically defined by requesting that for a given metric space (M, d) and a discrete set of atomic positions $\{s_1, s_2, \ldots\} \subset M$, the Voronoi cell of an atom fulfills

$$V(s_i) = \{x \in M |\, d(x, s_i) \leqslant d(x, s_j)\} \;\; \forall\, i \neq j. \tag{8}$$

The resulting distributions of the occupied volume (Voronoi cell) are displayed in Fig. 12 for both compositions NG2 [Fig. 12(a)] and N2G [Fig. 12(c)]. These exhibit a bimodal shape where the Ge atoms' lowest occupied volume contribution (17 Å^3) arises. Since their relative amount decreases with Na content, their contribution decreases substantially for N2G. We then calculate only the occupied volume distributions for the network species (Ge, S), revealing a dramatic change between NG2 and N2G. In the former, the differences in occupied volumes between the whole system and the network are barely visible [Figs. 12(a) and 12(b)], and both distributions have almost the same profile. Conversely, N2G indicates that Na ions occupy essentially large volumes, of about 27–32 Å^3, as the contributions in this volume range are absent if only network species are considered. This means that the available free volume for ion motion is more significant in such highly depolymerized glasses and cannot be originated by a change in density, i.e., $\rho_0 = 0.0403$ Å^{-3} and 0.0420 Å^{-3} for NG2 and N2G, respectively [3]. The fraction of available free volume for ion motion can be precisely calculated from the Voronoi distribution and is equal to 26.8% in NG2 and 49.1% in N2G, i.e., in Na-rich glasses, lots of space can be used for ionic motion.

C. Diffusivities

Figure 13(a) represents the mean-square displacement $\langle r^2(t)\rangle$ of the Na particles for the simulated temperatures, i.e., from 300 K (blue curve) to 1500 K (red) :

$$\langle r^2(t)\rangle(t) = \left\langle \frac{1}{N_{\mathrm{Na}}} \sum_{j=1}^{N_{\mathrm{Na}}} |\mathbf{r}_j(t) - \mathbf{r}_j(0)|^2 \right\rangle. \tag{9}$$

The usual features of $\langle r^2(t)\rangle$ are recovered, i.e., a short time ($t \leqslant 0.1$ ps), the Na motion is ballistic [71] and $\langle r_k^2(t)\rangle$ scales as t^2. At the same time, a diffusive regime sets in a long time and elevated temperature and is characterized by $\langle r_k^2(t)\rangle \propto t$. Although the mean-square displacement at 300 K has been represented (and 600 K to a lesser extent), the data are, by all means, useless [8] for the determination of a diffusion constant as the motion is now trapped in cages that extend beyond the available computer time limit. This manifests by a near plateau value at $\simeq$0.25 Å^2, providing a typical length scale for the cages. For the more elevated temperatures, the diffusive regime is clearly visible [broken line, Fig. 13(a)] and can now be characterized by a diffusion constant D, which is determined from

$$D = \frac{1}{6} \lim_{t\to\infty} \frac{d\langle r^2(t)\rangle}{\mathrm{d}t}. \tag{10}$$

An additional feature that is characteristic of modified silicates [43,72] is the significant difference in dynamics between the network-forming species and the Na ions [inset of Fig. 13(a)]. In the diffusive regime, this leads to an increasing diffusivity difference, up to at least one order of magnitude, with decreasing temperature [Fig. 13(b)], and provides the picture of "fast"-moving ions within a frozen network matrix. The representation [Fig. 13(b)] suggests an Arrhenius behavior for all particles, that is, $D \propto \exp[-E_A/k_BT]$ over an extended temperature range, indicative of a dynamics of activated type. An Arrhenius fit over temperatures 900–1500 K leads to $E_A = 0.31$ and 0.33 eV for the compositions N2G and NG2, respectively. At low temperature (600 K), a noticeable

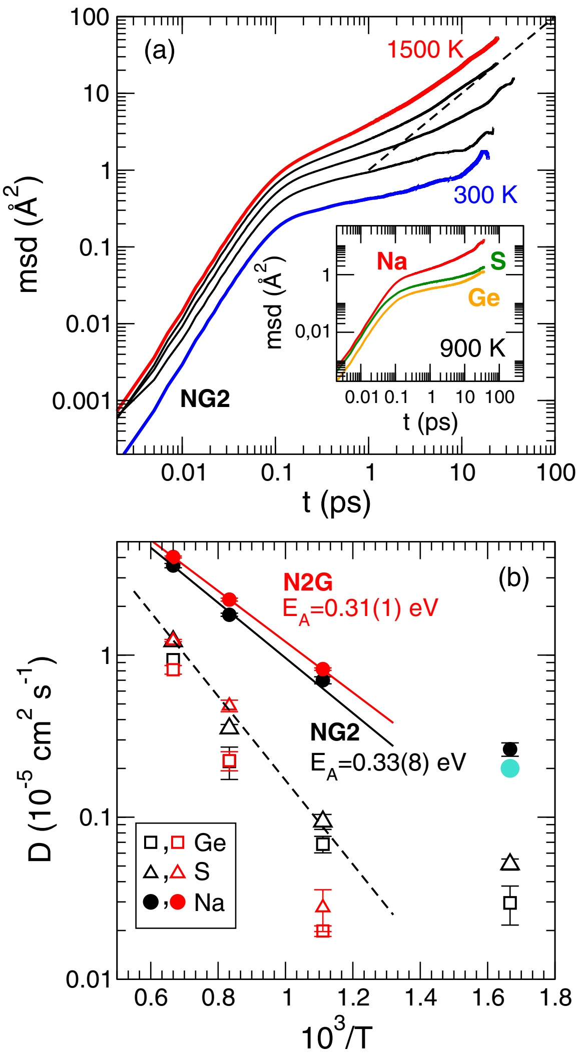

FIG. 13. (a) Mean-square displacement (msd) of Na particles in NG2 liquids and glasses. The broken line corresponds to the diffusive behavior at long times (slope of 1 in a log-log plot). The inset shows the msd of the three species in NG2 at 900 K. (b) Arrhenius plot of calculated diffusivities in NG2 (black) and N2G (red) liquids together with select Arrhenius fits (lines) and the corresponding activation energies E_A for sodium diffusivities. Filled circles, open boxes, and open triangles represent sodium, germanium, and sulfur data. A data point is provided from a FPMD simulation of NG supercooled liquid [8] (light blue).

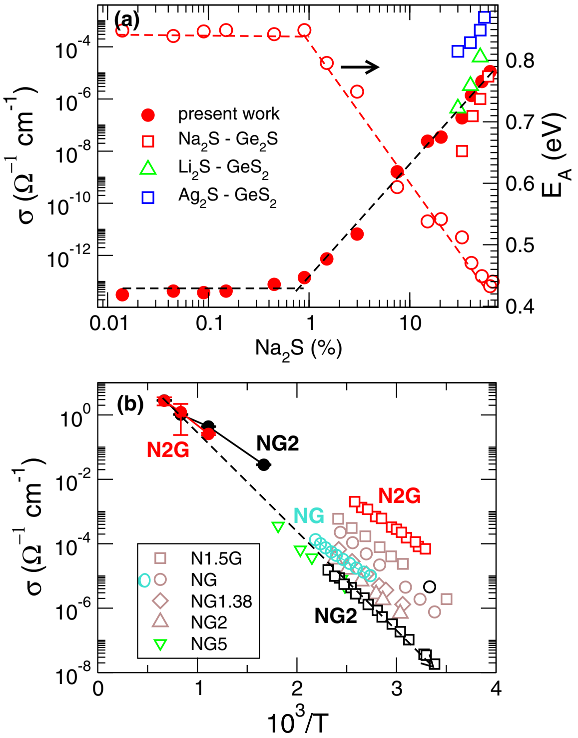

FIG. 14. (a) Measured conductivity at 300 K and activation energies E_A (right panel) with sodium content, together with data from other modified thiogermanates [4]. (b) Calculated [Eq. (11), filled circles] and measured (open symbols) ionic conductivity of NG2 (black) and N2G systems (red), together with experimental data for NG glasses [8] (cyan) and different compositions of NG (brown symbols [2]) and NG5 (green triangles [12]). An estimate using the Nernst-Einstein equation and calculated Na diffusivities is also represented.

deviation from the high-temperature Arrhenius behavior sets in that might be the result of a too-short simulation time [see Fig. 13(a)], albeit the calculation of D has been performed over the time interval satisfying $t > 10$ ps and over which $\langle r^2(t)\rangle$ displays a linear behavior in the log-log plot.

Our diffusivity data appear to be consistent with a rough evaluation from numerical simulations at 600 K [8] in the same system but at a different composition [50Na$_2$S-50GeS$_2$, NG, Fig. 13(b)], and also compatible with a measured sodium diffusivity from ^{22}Na tracer measurement at a lower temperature, 6×10^{-12} cm^2 s^{-1} for $10^3/T = 2.23$. Other data from sulfides lead to comparable diffusivities [73,74] such as GeS$_2$-Ag$_2$S or Na$_2$S-As$_2$S$_3$. A recent simulation of a slightly different sulfide (sodium thiosilicate) has led to diffusivities [75] and activation energies ($E_A = 0.258$ eV), which are also consistent with our estimates. However, the lower value of E_A leads to enhanced ease of sodium diffusion in Si-based glasses, consistent with the current observation [76–78] that conductivities in thiosilicates are higher than in thiogermanates.

D. Experimental conductivities

Figure 14(a) displays the dependence of the measured electrical conductivity of xNa$_2$S-(100-x)GeS$_2$ glasses at room temperature. The composition domain varies from very few percent in cation up to several tenths of a percent (from 0.01% to 66.6% Na$_2$S). The data clearly show two different conductivity regimes. The first regime corresponds to conductivity values of the order of 10^{-14} Ω^{-1} cm^{-1} for glasses containing between 0.01% and 1.0% Na$_2$S, and having a network structure very close to the one of GeS$_2$. An apparent change in conductivity is acknowledged at about $x_c \simeq 1.0\%$. Upon further addition, an increase of 8–9 orders of magnitude is estimated for the richest sodium glass (N2G) with a conductivity value as high as 4.25×10^{-4} Ω^{-1} cm^{-1}. The observed trend with composition [Fig. 14(a)] suggests some threshold behavior with a power law of the form $\sigma \simeq \sigma_0(x - x_c)^\alpha$

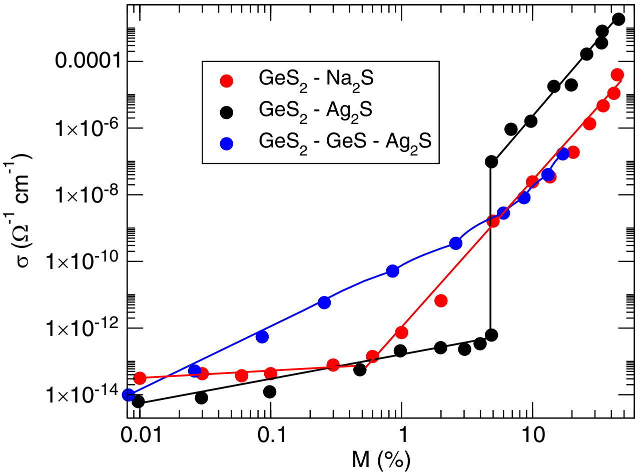

FIG. 15. Experimental ionic conductivities in GeS_2-Na_2S (M = Na) as a function of modifier content [same as Fig. 14(b)], and compared to GeS_2-Ag_2S (M = Ag) and GeS_2-GeS-Ag_2S (M = Ag).

for $x > x_c$ for the high conductivity region. The temperature dependence of the conductivity follows an Arrhenius $\sigma_T = \sigma_0 \exp[-E_A^\sigma/k_BT]$ typical of ionic glassy conductors below the glass transition temperature [79] [Fig. 14(b)]. A fit of such conductivity data allows us to determine the preexponential factor σ_0 and the activation energy for ionic conduction E_A^σ.

Figure 14(a) (right axis) represents this activation energy as a function of sodium content, and E_A^σ decreases with increasing network modifier. As for the conductivity, two different regimes ($x < x_c$ and $x > x_c$) are observed. Although the activation energy values are almost constant and equal to $E_A^\sigma = 0.85$ eV for $x < x_c$, these values decrease to 0.44 eV for the glass that contains the highest sodium content (N2G). The activation energy for ionic conduction is usually [32] the sum of a Coulombic contribution E_c (i.e., the energy barrier to create a free carrier) and migration energy E_m that is related to ionic motion, i.e., diffusion. The comparison of the calculated activation energy E_A for diffusivity [Fig. 13(b)], which does not vary significantly with Na content, and the one for ionic conduction E_A^σ permits to roughly estimate an average Coulomb energy for free carriers. We find $E_c = 0.10$–0.12 eV for NG2 and N2G, suggesting a near-independent effect of Na content on the energy barriers controlling the free carriers. Are there features specific to sodium thiogermanates? Figure 15 compares our results (red symbols) with the conductivities of the Ag_2S-GeS_2 and Ag_2S-GeS-GeS_2 glasses as a function of the mobile cation content M (M = Na, Ag). In Ag_2S-GeS_2 glasses, the conductivity data clearly showed two different conductivity domains, with a transition behavior involving a jumplike increase of 4 to 5 orders of magnitude in the conductivity occurring at about 8 at.% in silver. According to Balan *et al.* [80], SEM and electrostatic force (EFM) micrographs highlighted chemical and electrical heterogeneities related to phase separation, showing that the change in conductivity regime occurs when the regions of the Ag-rich phase start to connect in either (percolation threshold). In contrast, the conductivity of the $(Ag_2S)_x(GeS)_{60}(GeS_2)_{40-x}$ with different content in silver does not show any jump in conductivity when the amount of silver changes and homogeneous glasses were observed leading to a smooth increase of σ. According to the trends observed (Fig. 15), the conductivity dependence of the present Na_2S-GeS_2 glasses appears to be intermediate between the two Ag-based systems as there is no conductivity transition but two different regimes. There might, therefore, also be aspects of phase separation present in the thiogermanates, as discussed below (Sec. III E 2) from the numerical results.

E. Calculated conductivities

The measured conductivities in the glassy state can then be compared with a direct calculation of $\sigma(T)$ from the diffusivities [Fig. 13(b)] using:

$$\sigma(T) = \frac{(e)^2}{Vk_BT}\sum_j Z_j^2 D_j(T), \tag{11}$$

where V and Z_j are the system's volume, and Z_j is the charge of the species j with diffusivity D_j.

1. Overall behavior

The results are represented in Fig. 14(b) and indicate that at high temperature, the effect of the Na content is weak, as both compositions lead to similar values, e.g., $\sigma \simeq 5.0\ \Omega^{-1}\,\mathrm{cm}^{-1}$ at 1500 K. Because of the reduction of all energy barriers, the effect of the network is small. It leads to similar dynamics for all species [i.e., similar diffusivities, Fig. 13(b)]. The calculated values are compatible with those determined experimentally, i.e., an Arrhenius extrapolation of the low-temperature behavior [broken line, Fig. 14(b)] connects, indeed, the experimental and theoretical data sets. This qualitative agreement does not take into account the fact that one usually has an Arrhenius crossover in the glass transition region (here $T_g = 538$–551 K [4]), which reflects the fact that, similarly to other glass-forming electrolytes [79,81–84], conductivity is enhanced once the underlying network softens with the reduction of viscosity.

2. Evidence for a channel dynamics

A typical feature of modified network glasses such as alkali silicates (Na_2O-SiO_2) is the presence of channel dynamics for the ions, e.g., Na move along preferential pathways [85,86] within the structure. The presence of these channels leads to an obvious signature in quasielastic neutron scattering experiments [87,88], and manifests by a prepeak in the partial Na-Na structure factor $S_{\text{Na-Na}}(k)$ at $k_{PP} = 0.9$ Å^{-1}. Sodium-rich regions involve, in fact, a characteristic length scale of $\simeq$7 Å detected within a nearly frozen silica matrix. This has been documented for different compositions, and since alkali ions break the intertetrahedral Si-O-Si bond and depolymerize the structure [11], Na clustering emerges and leads to percolating channels [89] that are already present [90] for 20% Na_2O in binary sodium silicate glasses. Given that the present thiogermanates are isochemical (a group IV network former disrupted by Na ions), it is interesting to verify if there are also such features that have been characterized from MD simulations in the oxides [43,90–92]. We follow here the analysis performed by Meyer *et al.* [87], and focus on the partial Na-Na structure factor $S_{\text{Na-Na}}(k)$ (Fig. 16), which we find to exhibit a

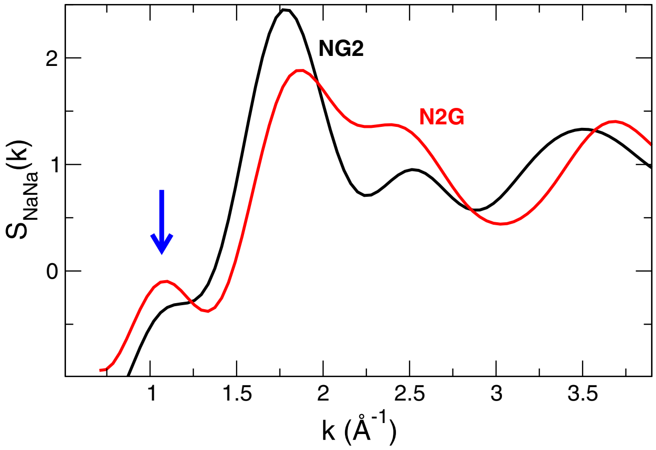

FIG. 16. Calculated Na-Na correlations $S_{\mathrm{Na\text{-}Na}}(k)$ in reciprocal space for the glasses NG2 (black) and N2G (red). The arrow indicates the prepeak around $k_{PP} = 1.05$ Å^{-1}.

well-defined prepeak at $k \simeq 1.05$ Å^{-1} for N2G. As for sodium silicates, the presence of this prepeak is the signature that some ordering of Na ions occurs and involves a typical length scale [93] of $7.7/k_{PP} \simeq 7$ Å.

Unlike silicates, with low modification (i.e., NG2), there is no real evidence for Na channels within the thiogermanate base structure as only a small shoulder is found to the principal peak at 1.75 Å^{-1}, and this is compatible with the weak differences in the structure functions between GeS_2 and NG2 (Fig. 2) and a visual inspection of the atomic structure (Fig. 1). The prepeak now becomes evident at significant Na content (N2G, red curves) and signals the presence of channels for Na motion, i.e., features of phase separation at the nanoscale with evident Na-rich subregions.

F. Vibration density of states

Figure 17 represents the vibrational density of states (VDOS) for both systems, defined by the Fourier transform of the velocity-velocity autocorrelation function $\langle \mathbf{v}(t) \cdot \mathbf{v}(0) \rangle$:

$$g(\omega) = \frac{1}{3Nk_BT} \sum_{j=1}^{N} \int_0^\infty \langle \mathbf{v}_j(t) \cdot \mathbf{v}_j(0) \rangle e^{i\omega t} dt, \qquad (12)$$

where N, k_B, and T are the total number of atoms, the Boltzmann constant, and the temperature, respectively.

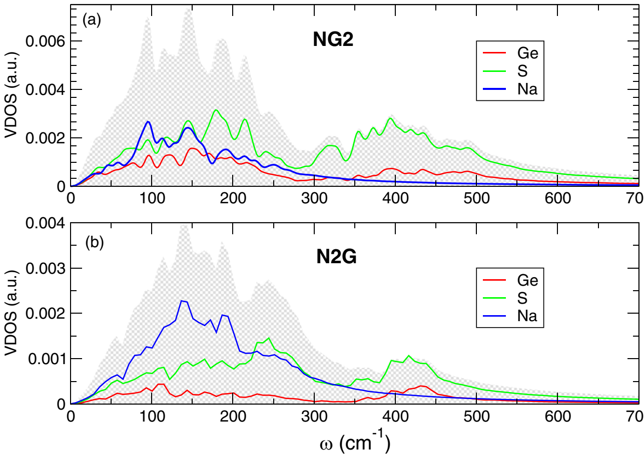

FIG. 17. Calculated vibrational density of states in NG2 (a) and N2G glasses (gray zones) together with the contributions from Ge (red), S (green), and Na (blue).

The VDOS of the GeS_2-rich system (NG2) consists of two broad bands found at $\omega < 300$ cm^{-1} and 300 cm^{-1} $< \omega <$ 600 cm^{-1} [Fig. 17(a)] and can be associated with vibrations of the different species, once the evaluation is performed individually for Ge, S, and Na atoms. With increasing Na content, the VDOS shifts to lower frequencies, and the first band becomes dominant for the N2G system. This is consistent with the fact that lower frequencies are usually associated with soft (floppy) modes [94] that emerge in such glasses for $x > 20\%$ [11], and the present simulation indicates that these are associated with Na atoms in N2G [Fig. 17(b)]. Conversely, the high-frequency band is dominated by the S atoms, and this feature appears to be nearly independent of composition. The present results complement those obtained in an early study of Raman spectroscopy [2,3], and also provide an additional insight. Here, bands near 340 cm^{-1} which are very intense [95] in GeS_2 were identified to be related to stretch vibrations of BS atoms in the thiogermanates. Note that a slightly higher frequency ($\simeq$390 cm^{-1}) has been determined [5] for NG2 in a more recent study, also confirmed independently [6]. This appears to be consistent with our results as the region between 300 and 400 cm^{-1} is dominated by the sulfur atoms (green curves, Fig. 17), and an obvious reduction of their intensity is acknowledged when moving from NG2 to N2G which is compatible with the reduction of BS atoms in depolymerized networks. Similarly, the observed high-frequency bands ($\simeq$480 cm^{-1}) were found to shift [2] to lower frequency between $33Na_2S$-$67GeS_2$ to $60Na_2S$-$40GeS_2$, and this effect is also detected as a global reduction of the S-related VDOS is acknowledged between NG2 and N2G. The recent Raman and infrared spectroscopic data [5] also assign high frequencies ($\simeq$465 cm^{-1}) to NBS stretching vibrations.

IV. SUMMARY AND CONCLUSIONS

Here, we have investigated experimentally and theoretically the structural, dynamic, and electric properties of different compositions in the GeS_2-Na_2S amorphous system, which serves as a base material for glassy electrolytes and might represent a very promising candidate for all-solid-state battery applications. In contrast to their oxide counterparts, sodium germanates, which have received considerable attention, such glassy materials received only a limited one, the investigation of conductivity tracing back to the beginning of the 1980s [3]. Recent experimental effort [7,8] and the discovery of the superionic nature of LGPS (Li-Ge-P-S)-type materials [96] ($Li_{10}GeP_2S_{12}$) using a combination of GeS_2 and P_2S_5 have brought a renewed and stimulating attention to the alkali-related binaries such as Na_2S-GeS_2 or Li_2S-GeS_2 [45].

Adding Na_2S into the base GeS_2 glass induces various structural changes that have been characterized by a combination of x-ray scattering, first-principles molecular dynamics, and electric measurements. Results indicate a deep network modification between 33% (NG2) and 66% (N2G) added Na_2S. While the former displays structure functions [$S(k)$ and $g(r)$] which are still similar to those of the base network GeS_2 and reveal a network character that is nearly maintained, the latter leads to a complete disruption with vanishing of medium-range elements (rings) and the promotion of voids that will facilitate conduction. The tetrahedral character of Ge atoms remains unchanged with a Q^n speciation similar to that of corresponding oxides or thiosilicates. Upon evolution from a Q^4 network (GeS_2) to a nearly Q^0 network (isolated molecules), the connection between the Ge tetrahedra is substantially modified with a collapse of ES elements and the presence of some dimer CS fragments in N2G, together with the presence of homopolar Ge-Ge bonds.

Conductivity results indicate that N-G glasses display a threshold behavior at very small composition, typically 1% Na_2S, similarly to other sulfide glasses, and then evolve as a power law up to about $10^{-4}\ \Omega^{-1}\,\mathrm{cm}^{-1}$ at 66% added Na_2S. These ultimate values for highly depolymerized glasses are slightly lower than those found in other modified sulfides [4]. With temperature, the conductivities display an Arrhenius behavior and eventually extrapolate to the values calculated in the liquid state from the molecular dynamics simulations. The nature of the dynamics is probed using the latter. It reveals that motion through channels has a structural signature, the significant increase of free volume accessed from a Voronoi analysis being probably responsible for the increase observed in glass conductivity between 33% and 66% added modifier. Taken together, these results appear now helpful in decoding isochemical (Na_2S-SiS_2) or other analogous glassy materials. They might also help to understand more complex glassy electrolytes using mixed modifier or network former, such as, e.g., Li_2S-GeS_2-P_2S_5 or Na_2S-SiS_2-GeS_2.

ACKNOWLEDGMENTS

M.M. acknowledges Chaire d'Excellence UNAM-Sorbonne Université for financial support and repeated funding from CNRS and Sorbonne Université. He also acknowledges supercomputing access to the cluster Romeo from Université de Reims Champagne-Ardennes. M.M., L.M.P., and A.P. acknowledge support from Fondation MAIF pour la recherche. Ongoing discussions with G. Naumis, H. Flores-Ruiz, P. Boolchand, and S. Sørensen are gratefully acknowledged.

[1] Z. A. Grady, C. J. Wilkinson, C. A. Randall, and J. C. Mauro, Front. Energy Res. **8**, 218 (2020).
[2] B. Barrau, M. Ribes, M. Maurin, A. Kone, and J.-L. Souquet, J. Non-Cryst. Solids **37**, 1 (1980).
[3] M. Ribes, B. Barrau, and J. Souquet, J. Non-Cryst. Solids **38-39**, 271 (1980).
[4] J. Souquet, E. Robinel, B. Barrau, and M. Ribes, Solid State Ionics **3-4**, 317 (1981).
[5] C. Bischoff, K. Schuller, N. Dunlap, and S. W. Martin, J. Phys. Chem. B **118**, 1943 (2014).
[6] Z. H. Zhou, K. Kamiya, K. Tsutsumi, T. Hashimoto, and H. Nasu, Phys. Chem. Glasses **40**, 146 (1999).
[7] K. Itoh and T. Fukunaga, Solid State Ionics **180**, 351 (2009).
[8] M. Kassem, T. Bounazef, A. Sokolov, M. Bokova, D. Fontanari, A. C. Hannon, I. Alekseev, and E. Bychkov, Inorg. Chem. **61**, 12870 (2022).
[9] I. L. B. Mykaylo, V. Lazarev, E. Yu. Peresh, and Z. Z. Kish, Russian J. Inorganic Chemistry **39**, 2319 (1989).
[10] P. Richet, M. Roskosz, and J. Roux, Chem. Geol. **225**, 388 (2006).
[11] M. Micoulaut, Am. Mineral. **93**, 1732 (2008).
[12] E. Plumat, J. Am. Ceram. Soc. **51**, 499 (1968).
[13] M. Micoulaut, Phys. Rev. B **74**, 184208 (2006).
[14] A. Pradel and A. Piarristeguy, C. R. Geosci. **354**, 79 (2022).
[15] Z. H. Zhou, H. Nasu, T. Hashimoto, and K. Kamiya, J. Non-Cryst. Solids **215**, 61 (1997).
[16] H. Tawarayama, E. Ishikawa, K. Yamanaka, K. Itoh, K. Okada, H. Aoki, H. Yanagita, Y. Matsuoka, and H. Toratani, J. Am. Ceram. Soc. **83**, 792 (2000).
[17] K. Tanaka, N. Nemoto, and H. Nasu, Jpn. J. Appl. Phys. **42**, 6748 (2003).
[18] S. Blaineau, S. Le Roux, and P. Jund, J. Phys.: Condens. Matter **19**, 455207 (2007).
[19] S. Le Roux, Ph.D. thesis, Université Montpellier II-Sciences et Techniques du Languedoc, 2008.
[20] S. Le Roux and P. Jund, Verres **15**, 54 (2009).
[21] S. Blaineau, P. Jund, and D. A. Drabold, Phys. Rev. B **67**, 094204 (2003).
[22] J. Harris, Phys. Rev. B **31**, 1770 (1985).
[23] M. Celino, S. Le Roux, G. Ori, B. Coasne, A. Bouzid, M. Boero, and C. Massobrio, Phys. Rev. B **88**, 174201 (2013).
[24] S. Chakraborty, P. Boolchand, and M. Micoulaut, Phys. Rev. B **96**, 094205 (2017).
[25] O. Masson, PYTSREDX, a data reduction program to obtain the atomic pair distribution function (pdf) from x-ray total scattering data (2022).
[26] http://ftp.esrf.fr/pub/scisoft/xop2.3/dabaxfiles/.
[27] A. K. Soper and P. Egelstaff, Nucl. Instrum. Methods **178**, 415 (1980).
[28] R. Car and M. Parrinello, Phys. Rev. Lett. **55**, 2471 (1985).
[29] A. Zeidler, J. W. Drewitt, P. S. Salmon, A. C. Barnes, W. A. Crichton, S. Klotz, H. E. Fischer, C. J. Benmore, S. Ramos, and A. C. Hannon, J. Phys.: Condens. Matter **21**, 474217 (2009).
[30] A. D. Becke, J. Chem. Phys. **96**, 2155 (1992).
[31] C. Lee, W. Yang, and R. G. Parr, Phys. Rev. B **37**, 785 (1988).
[32] M. Micoulaut, R. Vuilleumier, and C. Massobrio, Phys. Rev. B **79**, 214205 (2009).
[33] C. Massobrio, M. Micoulaut, and P. S. Salmon, Solid State Sci. **12**, 199 (2010).
[34] A. Bouzid, C. Massobrio, M. Boero, G. Ori, K. Sykina, and E. Furet, Phys. Rev. B **92**, 134208 (2015).
[35] A. Bouzid, S. Le Roux, G. Ori, M. Boero, and C. Massobrio, J. Chem. Phys. **143**, 034504 (2015).
[36] S. F. Boys and P. O. Löwdin, *Quantum theory of atoms, molecules, and the solid state* (Academic Press, New York, NY, 1966) 253.

[37] D. Marx and J. Hutter, *Ab Initio Molecular Dynamics: Basic Theory and Advanced Methods* (Cambridge University Press, Cambridge, 2009).

[38] G. H. Wannier, Phys. Rev. **52**, 191 (1937).

[39] N. Marzari and D. Vanderbilt, Phys. Rev. B **56**, 12847 (1997).

[40] P. L. Silvestrelli, N. Marzari, D. Vanderbilt, and M. Parrinello, Solid State Commun. **107**, 7 (1998).

[41] M.-P. Gaigeot, R. Vuilleumier, M. Sprik, and D. Borgis, J. Chem. Theory Comput. **1**, 772 (2005).

[42] B. Rotenberg, M. Salanne, C. Simon, and R. Vuilleumier, Phys. Rev. Lett. **104**, 138301 (2010).

[43] M. Bauchy and M. Micoulaut, Phys. Rev. B **83**, 184118 (2011).

[44] M. Micoulaut, J. Phys.: Condens. Matter **31**, 285402 (2019).

[45] K. Itoh, Solid State Ionics **383**, 115986 (2022).

[46] P. S. Salmon, J. Non-Cryst. Solids **353**, 2959 (2007).

[47] M. Micoulaut and P. Boolchand, Front. Mater. **6**, 283 (2019).

[48] G. S. Henderson, Can. Mineral. **43**, 1921 (2005).

[49] L.-M. Poitras and M. Micoulaut, Phys. Rev. B **107**, 214205 (2023).

[50] A. Pant, Acta Crystallogr. Sect. B **24**, 1077 (1968).

[51] W. T. McDonald and D. Cruickshank, Acta Crystallogr. **22**, 37 (1967).

[52] X. Yuan and A. N. Cormack, J. Non-Cryst. Solids **283**, 69 (2001).

[53] J. Du and A. Cormack, J. Non-Cryst. Solids **349**, 66 (2004).

[54] J. Du and L. R. Corrales, J. Chem. Phys. **125**, 114702 (2006).

[55] H. Uhlig, M. J. Hoffmann, H.-P. Lamparter, F. Aldinger, R. Bellissent, and S. Steeb, J. Am. Ceram. Soc. **79**, 2833 (1996).

[56] A. C. Hannon, B. Vessal, and J. M. Parker, J. Non-Cryst. Solids **150**, 97 (1992).

[57] L. Pauling, J. Chem. Educ. **69**, 519 (1992).

[58] E. D. Lacy, Phys. Chem. Glasses **6**, 171 (1965).

[59] H. Maekawa, T. Maekawa, K. Kawamura, and T. Yokokawa, J. Non-Cryst. Solids **127**, 53 (1991).

[60] M. Bauchy, J. Chem. Phys. **137**, 044510 (2012).

[61] M. Micoulaut, I. Pethes, P. Jóvári, L. Pusztai, M. Krbal, T. Wágner, V. Prokop, Š. Michalik, K. Ikeda, and I. Kaban, Phys. Rev. B **106**, 014206 (2022).

[62] K. Ohara, A. Mitsui, M. Mori, Y. Onodera, S. Shiotani, Y. Koyama, Y. Orikasa, M. Murakami, K. Shimoda, K. Mori *et al.*, Sci. Rep. **6**, 21302 (2016).

[63] S. Le Roux and P. Jund, Comput. Mater. Sci. **49**, 70 (2010).

[64] S. V. King, Nature (London) **213**, 1112 (1967).

[65] D. S. Franzblau, Phys. Rev. B **44**, 4925 (1991).

[66] P. M. Bridenbaugh, G. P. Espinosa, J. E. Griffiths, J. C. Phillips, and J. P. Remeika, Phys. Rev. B **20**, 4140 (1979).

[67] G. Dittmar and H. Schäfer, Acta Crystallogr. Sect. B **32**, 2726 (1976).

[68] M. Peters and L. McNeil, J. Non-Cryst. Solids **139**, 231 (1992).

[69] P. Boolchand, J. Grothaus, and J. Phillips, Solid State Commun. **45**, 183 (1983).

[70] P. H. Fuoss, P. Eisenberger, W. K. Warburton, and A. Bienenstock, Phys. Rev. Lett. **46**, 1537 (1981).

[71] J.-P. Hansen and I. R. McDonald, *Theory of Simple Liquids: With Applications to Soft Matter* (Academic, New York, 2013).

[72] M. Bauchy, B. Guillot, M. Micoulaut, and N. Sator, Chem. Geol. **346**, 47 (2013).

[73] E. Bychkov, Solid State Ionics **136-137**, 1111 (2000).

[74] I. Alekseev, D. Fontanari, A. Sokolov, M. Bokova, M. Kassem, and E. Bychkov, *Ionic Conductivity and Tracer Diffusion in Glassy Chalcogenides*, Vol. 1 (World Scientific, Singapore, 2020).

[75] S. r. Sørensen, M. Micoulaut, and M. Smedskjaer (unpublished).

[76] V. Desphande, A. Pradel, and M. Ribes, Mater. Res. Bull. **23**, 379 (1988).

[77] A. Pradel and M. Ribes, Mater. Chem. Phys. **23**, 121 (1989).

[78] A. Pradel, C. Rau, D. Bittencourt, P. Armand, E. Philippot, and M. Ribes, Chem. Mater. **10**, 2162 (1998).

[79] M. Malki, V. Magnien, O. Pinet, and P. Richet, Geochim. Cosmochim. Acta **165**, 137 (2015).

[80] V. Balan, A. Piarristeguy, M. Ramonda, A. Pradel, and M. Ribes, J. Optoelectron. Adv. Mater **8**, 2112 (2006).

[81] D. Golodnitsky, E. Strauss, E. Peled, and S. Greenbaum, J. Electrochem. Soc. **162**, A2551 (2015).

[82] C.-H. Tu, L. Veith, H.-J. Butt, and G. Floudas, Macromolecules **55**, 1332 (2022).

[83] M. Aniya and M. Ikeda, Phys. Status Solidi B **257**, 2000139 (2020).

[84] H. Fan, L. Del Campo, V. Montouillout, and M. Malki, J. Non-Cryst. Solids **543**, 120160 (2020).

[85] C. Angell, P. Cheeseman, and S. Tamaddon, J. Phys. Colloq. **43**, C9-381 (1982).

[86] G. Greaves, J. Non-Cryst. Solids **71**, 203 (1985).

[87] A. Meyer, J. Horbach, W. Kob, F. Kargl, and H. Schober, Phys. Rev. Lett. **93**, 027801 (2004).

[88] A. Meyer, F. Kargl, and J. Horbach, Neutron News **23**, 35 (2012).

[89] H. Nesbitt, G. Henderson, G. Bancroft, and R. Ho, J. Non-Cryst. Solids **409**, 139 (2015).

[90] P. Jund, W. Kob, and R. Jullien, Phys. Rev. B **64**, 134303 (2001).

[91] T. Voigtmann and J. Horbach, Europhys. Lett. **74**, 459 (2006).

[92] E. Sunyer, P. Jund, and R. Jullien, Phys. Rev. B **65**, 214203 (2002).

[93] P. S. Salmon, Proc. R. Soc. London A **445**, 351 (1994).

[94] W. A. Kamitakahara, R. L. Cappelletti, P. Boolchand, B. Halfpap, F. Gompf, D. A. Neumann, and H. Mutka, Phys. Rev. B **44**, 94 (1991).

[95] L. Cai and P. Boolchand, Nanoscale phase separation of GeS2 glass, Philos. Mag. B **82**, 1649 (2002).

[96] N. Kamaya, K. Homma, Y. Yamakawa, M. Hirayama, R. Kanno, M. Yonemura, T. Kamiyama, Y. Kato, S. Hama, K. Kawamoto *et al.*, Nat. Mater. **10**, 682 (2011).